

New $\lambda 6$ cm observations of the Cygnus Loop

X. H. Sun¹, W. Reich², J. L. Han¹, P. Reich², and R. Wielebinski²

¹ National Astronomical Observatories, Chinese Academy of Sciences, Beijing 100012, PR China
e-mail: [xhsun;hjl]@bao.ac.cn

² Max-Planck-Institut für Radioastronomie, Auf dem Hügel 69, Bonn 53121, Germany
e-mail: [wreich;preich;rwiebinski]@mpi-fr-bonn.mpg.de

Received 31 August 2005 / Accepted 4 October 2005

ABSTRACT

Radio continuum and polarization observations of the entire Cygnus Loop at $\lambda 6$ cm wavelength were made with the Urumqi 25 m telescope. The $\lambda 6$ cm map is analysed together with recently published maps from the Effelsberg 100 m telescope at $\lambda 21$ cm and $\lambda 11$ cm. The integrated flux density of the Cygnus Loop at $\lambda 6$ cm is 90 ± 9 Jy, which implies a spectral index of $\alpha = -0.40 \pm 0.06$. This rules out any global spectral steepening up to $\lambda 6$ cm. However, small spectral index variations in some regions of the source are possible, but there are no indications for any spectral curvature. The linear polarization data at $\lambda 6$ cm show percentage polarizations up to 35% in some areas of the Cygnus Loop, exceeding those observed at $\lambda 11$ cm. The Rotation Measure is around -21 rad m^{-2} in the southern area, which agrees with previous observations. However, the distribution of Rotation Measures is rather complex in the northern part of the Cygnus Loop, where the $\lambda 21$ cm emission is totally depolarized. Rotation Measures based on $\lambda 11$ cm and $\lambda 6$ cm data are significantly larger than in the southern part. The difference in the polarization characteristics between the northern and southern part supports previous ideas that the Cygnus Loop consists of two supernova remnants.

Key words. ISM: magnetic fields – ISM: supernova remnants – radio continuum: ISM – techniques: polarimetric

1. Introduction

The Cygnus Loop (G74.0–8.5) is a large and intense non-thermal Galactic radio source. It is a rather well studied object at all observing bands. It has an apparent size of $\sim 4^\circ \times 3^\circ$ and its distance was recently revised to 540 pc by Blair et al. (2005) using *Hubble Space Telescope* data. The small distance and its location well out of the Galactic plane lead to little obscuration or confusion with Galactic emission. Its non-thermal radio spectrum makes its identification as a supernova remnant (SNR) most likely, which is supported by observations in other wavelength ranges.

In the radio band a recent spectral index study of the Cygnus Loop was made by Uyaniker et al. (2004) using high quality data from the Effelsberg 100 m telescope and the DRAO synthesis telescope in the frequency range from 408 MHz to 2675 MHz at arcmin angular resolution. For the integrated radio emission they obtained a spectral index of $\alpha = -0.42 \pm 0.06$ (with α defined as $S_\nu \propto \nu^\alpha$, with S_ν being the flux density and ν the frequency). This straight spectrum rules out any spectral break around 1 GHz as reported earlier (DeNoyer 1974). However, the flux density measured by Kundu & Becker (1972) at 5 GHz, the highest frequency where the Cygnus Loop was observed so far, is inconsistent with the spectrum of Uyaniker et al. (2004) and indicates some

spectral steepening above 2.7 GHz. A steepening in the spectrum of a SNR is an important and characteristic feature, which is closely connected to the age and the evolution of the source in the interstellar medium. This is for instance observed for the SNR S147, which is similar to the Cygnus Loop in many aspects (Fürst & Reich 1986). It is therefore of interest to establish the spectral break for the Cygnus Loop and to identify regions or structures within the SNR where the spectral break takes place. However, sensitive radio continuum observations of large sources like the Cygnus Loop are not easy to perform. Only single-dish telescopes can do that at high frequencies. However, they need a high sensitivity and baseline stability of the receiving system (a low 1/f-noise) so that any large-scale emission component is detected, otherwise it will lead to an underestimate of the integrated flux density and falsely suggest a steepening of the spectrum.

The Cygnus Loop is not fully understood, although it has been observed in almost all bands of the electromagnetic spectrum. In particular its morphology with a large northern circular shell and a bubble-like southern part makes it an unusual object compared to other SNRs. It was argued (Aschenbach & Leahy 1999) that the southern bubble resembles the out-break of the SNR as visible in the X-ray bright northern shell into a low density cavity of the interstellar medium. However, theoretical modeling by Tenorio-Tagle et al. (1985) assuming

a molecular environment shows that the SNR must have exploded in the southern bubble and the northern part is the out-break. Substantial differences between the northern part and the southern part have been observed in their radio emission properties (Uyaniker et al. 2004) as well as in their optical and X-ray emission characteristics (Patnaude et al. 2002). This motivated Uyaniker et al. (2002) to propose that the Cygnus Loop consists of two likely interacting SNRs: G74.3–8.4 and G72.9–9.0. That the Cygnus Loop consists of two SNRs was independently put forward by Leahy (2002). However, more data are needed to settle this view.

In this paper we try to resolve these questions using sensitive $\lambda 6$ cm observations of this large radio source made with a new $\lambda 6$ cm receiving system installed at the Urumqi 25 m telescope. We describe the receiving system and the data reduction procedure in some detail in Sect. 2. Our results and the analysis of the total intensity and polarized emission of the Cygnus Loop at $\lambda 6$ cm, 11 cm and 21 cm are presented in Sect. 3, followed by remarks on the two-SNR scenario and the conclusion in Sects. 4 and 5, respectively.

2. Observations and data reduction

The $\lambda 6$ cm observations were made with the 25 m telescope at Nanshan station operated by the Urumqi Astronomical Observatory, which is part of the National Astronomical Observatories of the Chinese Academy of Sciences. The telescope is located about 70 km south of Urumqi city at an altitude of 2029 m above sea level with the geographic longitude of 87°E and latitude of $+43^\circ$. The telescope was mainly used for VLBI observations as a member of the European VLBI Network and also for pulsar timing observations at L -band (Wang et al. 2001, 2003). New possibilities for continuum and polarization mapping were opened by the recent installation of a dual-channel $\lambda 6$ cm receiving system constructed at the Max-Planck-Institut für Radioastronomie (MPIfR) in Bonn/Germany. This receiver is a copy of the $\lambda 6$ cm receiver in operation at the MPIfR Effelsberg 100 m telescope since 1996. The new receiver has a higher stability and a lower $1/f$ -noise, which are ideal characteristics to perform mapping of large areas of the sky in the radio continuum and in linear polarization.

The $\lambda 6$ cm receiver is installed at the secondary focus of the 25 m telescope. Following the corrugated circular feed horn an orthogonal transducer converts the signal into left-hand (L) and right-hand (R) circularly polarized components, which are then amplified by two cooled HEMT pre-amplifiers working below 15 K. A “Digital Backend” from the MPIfR collects the data at a sampling rate of 32 ms. Every 32 ms the frontend setting changes, so that either a calibration signal of $1.7\text{ K } T_a$ is added to the antenna signal and/or the signal phase is switched off by 180° . Four phases include all possible combinations in 4×32 ms. This fast switching ensures a continuous gain control of the receiving system and the 180° phase switch allows us to compensate for the quadratic terms of the IF-polarimeter, which is the same as those used at the Effelsberg 100 m telescope for broadband polarization observations (Wielebinski et al. 2002).

Table 1. Observational parameters for the Cygnus Loop.

Frequency [GHz]	4.8
Bandwidth [MHz]	600
T_{sys} [K]	22
$HPBW$ [']	9.5
Scan mode	RA and Dec
Scan-velocity [$^\circ/\text{min}$]	2
Scan separation [']	4
Map size [$^\circ \times ^\circ$]	4.2×4.8
Coverages I (PI) map	5 (6)
rms-I [mK]	1.0
rms-PI [mK]	0.4
Observation date	August–December 2004
Primary calibrator	3C 286
Flux density [Jy]	7.5
Polarization percentage [%]	11.3
Polarization angle [$^\circ$]	33

A computer with a LINUX operation system is used to store the raw data in the MBFITS format as developed for the Effelsberg 100 m, the IRAM 30 m and the APEX 12 m telescopes (Hatchell 2003). The raw data are further processed by the TOOLBOX-software package adapted from the Effelsberg 100 m telescope. Via TOOLBOX, the raw data of the four backend channels (RR*, LL*, RL*, LR*) are converted from a time series into a tabulated format with a user specified fixed spatial separation on the sky using a sinc-interpolation function. The calibration signals of each subscan (row or column) of a map are extracted and fitted to account for any gain drifting and also to control the phase stability of the IF polarimeter. The tabulated maps are then transformed into NOD2 maps (Haslam 1974) with the polarization U and Q -channels corrected for the parallactic angles. The LINUX PC is also used to command the telescope control computer to move the telescope according to the mapping requirements. Mapping can be done in a number of different astronomical coordinate systems and in the az/el coordinate system of the telescope.

From test observations made in August 2004 the relevant system and antenna parameters were determined. A detailed description of the system performance will be given elsewhere. In brief: the system temperature was measured to be about 22 K for clear sky conditions towards the zenith. The beam is circular and the half power beam width ($HPBW$) was found to be $9.5'$. The aperture efficiency was measured to be about 62% and the beam efficiency is about 67%. The maximum of the first sidelobes along the four feed support legs is about -17 dB or 2%. The conversion factor between Jy/beam area and the main beam brightness temperature is $T_B[\text{K}]/S[\text{Jy}] = 0.164$. The central frequency of the receiver is 4.8 GHz and its bandwidth is 600 MHz (see Table 1).

We made a number of 4.2×4.8 raster-scan maps of the Cygnus Loop area centered at $\alpha_{2000} = 20^{\text{h}}52^{\text{m}}$, $\delta_{2000} = 30^\circ30'$ by scanning along right ascension or declination direction, respectively. All these observations were done in autumn 2004

at clear sky. To avoid any contamination by the far-sidelobe response of the solar emission all the observations were conducted in the late evening or during the night. The scan velocity was always $2^\circ/\text{min}$. The scan spacing of $4'$ provides full sampling. This means 2 s of integration time for each pixel and about 153 min for one coverage. The tracking and pointing errors for each coverage are within $1'$ in right ascension and $30''$ in declination as found by fitting strong compact sources within the field and comparing with positions provided by the NVSS (Condon et al. 1998).

The NOD2 based data reduction package for radio continuum and polarization observations from the Effelsberg 100 m telescope was converted from the SOLARIS operation system to the LINUX system for Urumqi observations. The individual maps were edited to remove spiky interference, to correct baseline curvatures by polynomial fitting, and to suppress scanning effects by applying an “unsharp masking method” (Sofue & Reich 1979). All individual maps were on a relative baselevel, where the two ends of each subscan are set to zero. All maps observed in the two scanning directions were then “weaved” together by applying the method of Emerson & Gräve (1988), which is quite powerful to destripe a set of maps in the Fourier domain.

The flux density scale for the continuum and polarization observations and also the polarization angle was adapted to 3C 286 as the main calibrator (see Table 1). 3C 48 and 3C 138 were observed as secondary calibration sources, which were always visible during the Cygnus Loop observations. From the scatter of the measured calibration sources we quote an accuracy of our total intensity and polarized intensity scales of about 5%. The polarization angle is stable within $\pm 1^\circ$.

3. Result and analysis

3.1. Urumqi $\lambda 6$ cm map

From five full coverages of the Cygnus Loop and another partial one of its northern part we obtained the total intensity map as shown in the upper panel of Fig. 1. For the maps in Stokes U and Q we have one full coverage in addition. From the U and Q maps we then calculated the polarized intensity map corrected for the noise level and the distribution of polarization angles. The resultant rms-noise in our final total intensity map is about $1 \text{ mK } T_B$ and $0.3 \text{ mK } T_B$ in the Stokes U and Q maps and about $0.4 \text{ mK } T_B$ in the polarized intensity map. These rms-values are slightly larger than those expected from test observations of small fields, which can be attributed to “scanning effects” caused by instrumental drift, atmosphere and ground radiation variations that affect total intensity signals more severely than correlated polarization data. In addition, low-level interference close to the noise level cannot be easily identified, but may also lower the sensitivity. A Gaussian fit to strong sources in the map yield an effective angular resolution of $9'.7$, also slightly larger than test observations reflecting small pointing differences between different coverages. All relevant observational parameters are listed in Table 1. The final results of our $\lambda 6$ cm observation are shown in Fig. 1 slightly smoothed to a $HPBW$ of $10'$.

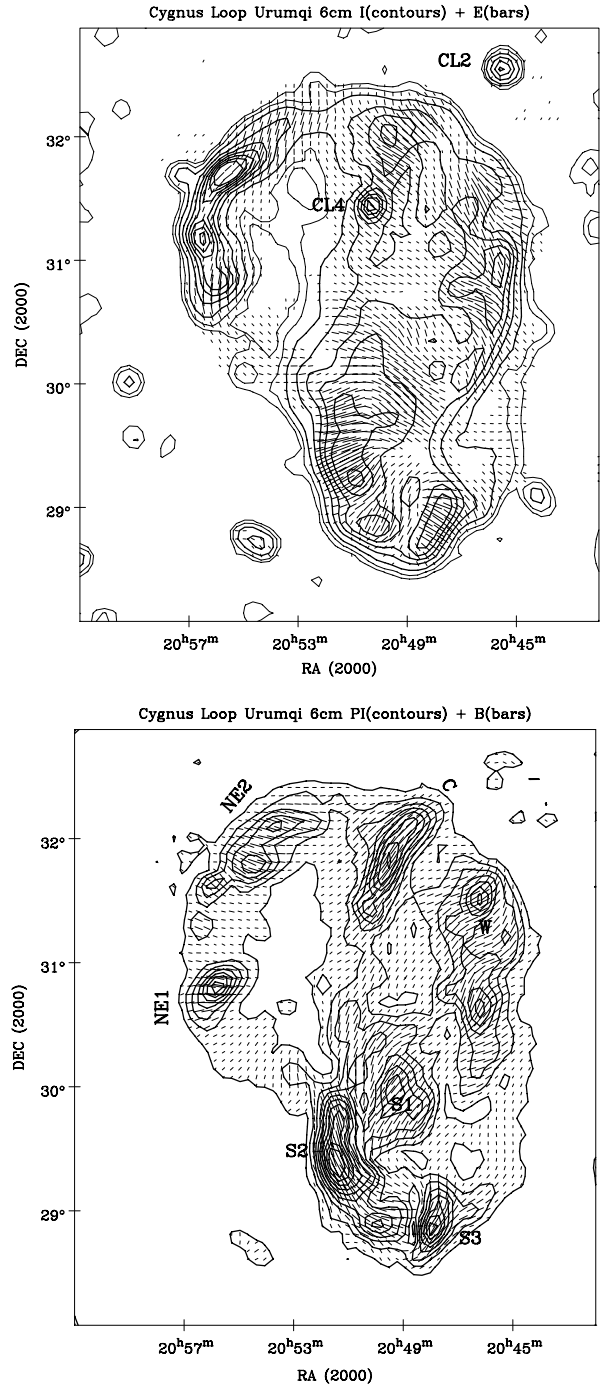


Fig. 1. The Urumqi $\lambda 6$ cm map of the Cygnus Loop smoothed to a $HPBW$ of $10'$. *Upper panel:* total intensity is displayed in contours, where the intensity levels of 5, 10 (thin lines), 20, 40, 60 $\text{mK } T_B$... (thick lines) are shown. The bars show the orientation of the polarization E -vectors with their length proportional to the polarized intensity and with the lower limit of $2 \text{ mK } T_B$ ($5 \times \text{rms-noise}$). The sources CL 2 and CL 4 are marked. *Lower panel:* contours show polarized intensities starting from $2 \text{ mK } T_B$ and running in $3 \text{ mK } T_B$ steps. The bars are the same as in the upper panel but show the orientation of the B -vectors by adding 90° (this assumes negligible Faraday rotation). The main polarized features are labeled.

During our observations we noted that the flux density of the source CL 4 (Fig. 1 upper panel, α_{2000} : $20^{\text{h}}50^{\text{m}}46^{\text{s}}.3$, δ_{2000} : $31^{\circ}27'51''.0$) (Keen et al. 1973) varied by about 30% during

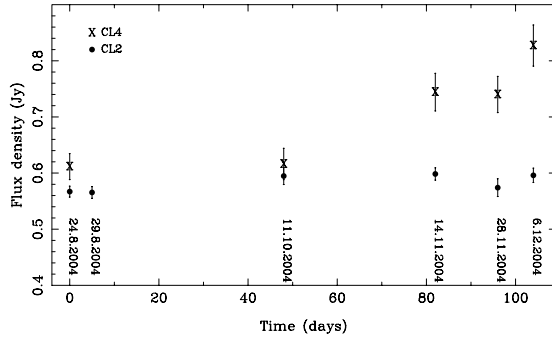


Fig. 2. The flux densities of CL 2 and CL 4 are plotted versus time. No flux density of CL 4 was obtained on August 29, 2004.

a timescale of about 48 days (Fig. 2). Attention to the variability of CL 4 was first drawn by Keen et al. (1973). Its location in the Cygnus Loop direction makes it a source of special interest. Meanwhile CL 4 was proved to be of extragalactic origin from H α absorption observation (Goss et al. 1979) with a redshift of 3.18 (Desai & Fey 2001). The observed variations cannot be explained by any instrumental effects since the simultaneous observation of CL 2 (Fig. 1 upper panel, α_{2000} : $20^{\text{h}}45^{\text{m}}44^{\text{s}}.2$, δ_{2000} : $32^{\circ}33'42''.5$) did not show any variation (Fig. 2). Apart from its high variability CL 4 shows angular broadening of the turbulent interstellar medium as discussed by Desai & Fey (2001). The flux density of 0.58 Jy for CL 2 is consistent with the spectral index of $\alpha = -0.48$ obtained by Keen et al. (1973) between 408 MHz and 2695 MHz.

3.2. Effelsberg maps at $\lambda 21$ cm and $\lambda 11$ cm

In the following we compare our new $\lambda 6$ cm Cygnus Loop map with those at $\lambda 21$ cm and $\lambda 11$ cm from the Effelsberg 100 m telescope. The $\lambda 21$ cm data were published by Uyaniker et al. (1999) as example maps for the Effelsberg ‘‘Medium Galactic Latitude Survey’’, where the Cygnus Loop area was cut out from a larger field. It should be noted, that the polarization data were meanwhile reprocessed to better account for instrumental cross talk effects. The differences to the published maps are small in general but only show up in areas of strong continuum sources. The $\lambda 11$ cm map was published by Uyaniker et al. (2002). Both Effelsberg maps were convolved to a common angular resolution of $10'$ to be compared with the Urumqi map. At this angular resolution we measure a noise level of 13 mK and 10 mK at $\lambda 21$ cm and 4 mK and 1.4 mK at $\lambda 11$ cm for total intensity and polarized intensity, respectively. The smoothed Effelsberg $\lambda 11$ cm and $\lambda 21$ cm maps are shown in Figs. 3 and 4, respectively.

3.3. The integrated flux density spectrum of the Cygnus Loop

We obtained an integrated flux density of the Cygnus Loop at $\lambda 6$ cm of 90 ± 9 Jy. To make the result compatible with previous values, we have included point sources in the flux integration. The quoted error reflects the uncertainties in determining the calibration factors and background levels, which adds up

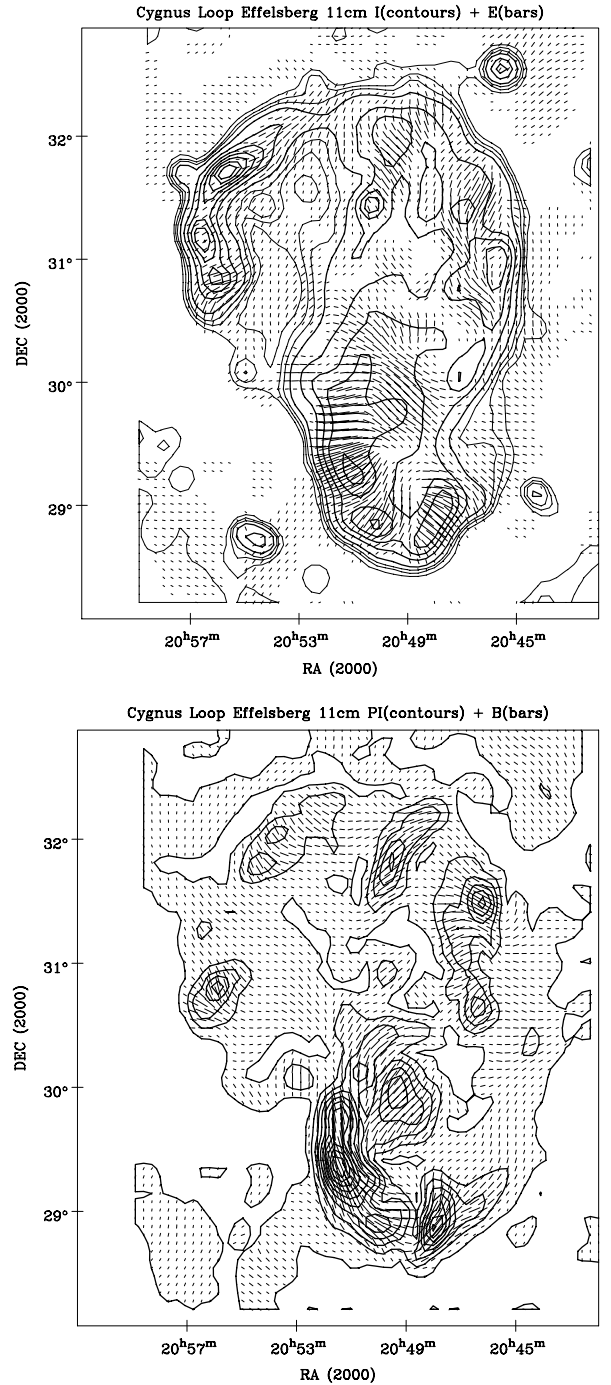


Fig. 3. The same as Fig. 1 but for the Effelsberg $\lambda 11$ cm maps. In the upper panel the thin contours start from 20 mK T_B with an interval of 20 mK T_B . The thick contours start at 100 mK T_B and run in 100 mK T_B steps of total intensity. In the lower panel, the polarization intensity contours start at 7 mK T_B and run in 14 mK T_B steps. Bars with polarization intensities below 7 mK T_B ($5 \times$ rms-noise) are not shown.

to about 10%. Combining our integrated $\lambda 6$ cm flux density with lower frequency data obtained recently by Uyaniker et al. (2004), we derived a spectral index of $\alpha = -0.40 \pm 0.06$ (Fig. 5). This is consistent with the result by Uyaniker et al. (2004), who derived $\alpha = -0.42 \pm 0.06$ up to $\lambda 11$ cm. There is no indication of a spectral break in the frequency range up

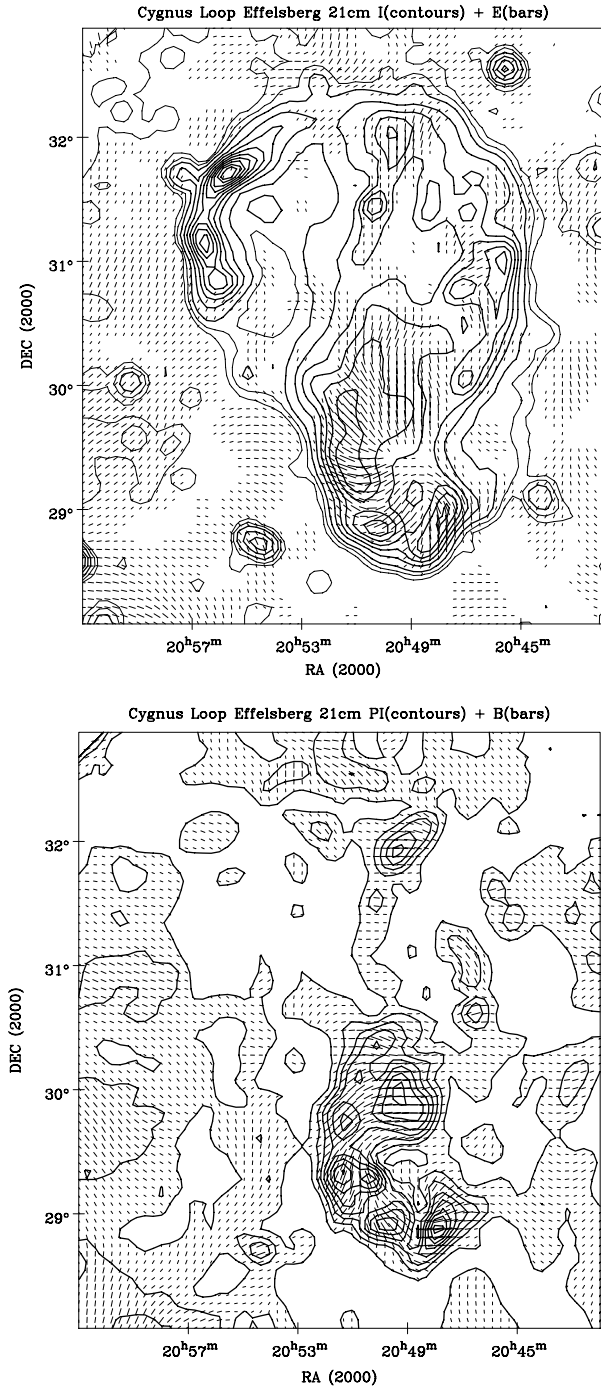


Fig. 4. The same as Fig. 3 but for the $\lambda 21$ cm maps. In the upper panel contours represent the total intensities. The thin contours are at 65 and 195 mK T_B and the thick contours at 400, 800, 1200 mK T_B ... In the lower panel polarization intensity contours at 50, 100, 150 mK T_B ... are shown. Bars with polarization intensity smaller than 50 mK T_B ($5 \times$ rms-noise) are not shown.

to $\lambda 6$ cm. The only $\lambda 6$ cm flux density of the Cygnus Loop previously obtained by Kundu & Becker (1972) was 73 ± 7 Jy. This flux density is lower than our result by 20% (see Fig. 5), which is probably caused by missing some diffuse emission due to the lower receiver sensitivity at that time compared to our present $\lambda 6$ cm system. Their low flux density was interpreted as an indication of a spectral steepening. However,

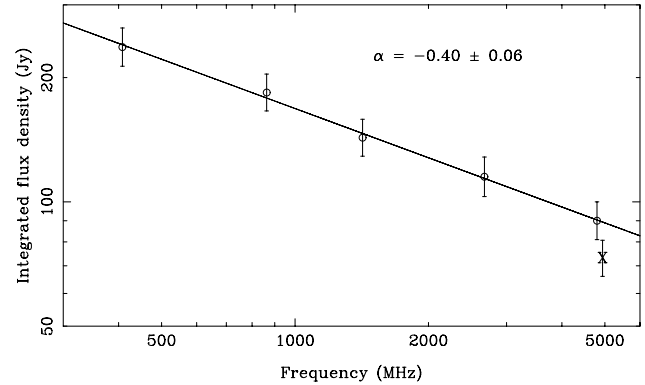


Fig. 5. The spectral index was calculated based on flux density values determined by Uyaniker et al. (2004) and the present $\lambda 6$ cm data. The result of Kundu & Becker (1972) is included for comparison and marked by “X”.

our new $\lambda 6$ cm measurements do not confirm this low flux density.

3.3.1. TT-plot analysis

We made temperature – versus – temperature (TT) plots of the entire source at $10'$ angular resolution between the Urumqi $\lambda 6$ cm and the Effelsberg maps at $\lambda 21$ cm and $\lambda 11$ cm to establish a common baselevel for these maps.

As the Cygnus Loop is very large, the diffuse Galactic emission is probably not constant across the entire source. This might cause offsets in the TT-plots in particular for low brightness temperatures. This effect might also increase the spectral index from TT-plots, since the spectrum of the Galactic emission is steeper. Therefore we have discarded all pixels with a brightness temperature below 10 mK T_B at $\lambda 6$ cm, 50 mK T_B at $\lambda 11$ cm, and 300 mK T_B at $\lambda 21$ cm when we fit spectral indices from TT-plots (Fig. 6).

According to the TT-plots, 2 mK, 8 mK, and 23 mK are added to the 4800 MHz, 2675 MHz and 1400 MHz maps. In addition the TT-plot yields the spectral index β between $\lambda 6$ cm/ $\lambda 11$ cm, $\lambda 6$ cm/ $\lambda 21$ cm, and $\lambda 11$ cm/ $\lambda 21$ cm data: $\beta = -2.43 \pm 0.04$, -2.46 ± 0.04 , and -2.47 ± 0.04 , respectively. The spectral index of the brightness temperature β and of the flux density α has the relation $\alpha = 2 + \beta$. The average spectral index $\alpha = -0.45 \pm 0.04$ derived from the TT-plot is consistent with the spectral index obtained from integrated flux densities.

3.3.2. Spectral index map of the Cygnus Loop

Using the maps with corrected background levels we calculated a spectral index map as shown in Fig. 7, where the spectral index of each pixel was obtained by linearly fitting the brightness temperatures at three frequencies. In order to achieve a high signal-to-noise ratio and to exclude the influence of systematic effects we took the similar cut-off levels as the TT-plots. Figure 7 shows some distinct regions with a higher than average spectral index: the northeastern rim (NGC 6992/5 or NE1/NE2 in Fig. 1) and the northwestern region (W in Fig. 1) both with spectral index of $\alpha \sim -0.40$, and the southern

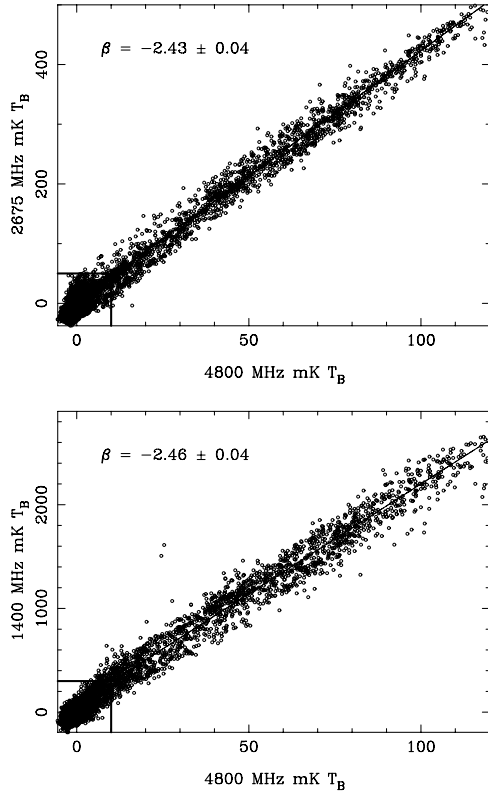


Fig. 6. The TT-plots of the $\lambda 6$ cm/ $\lambda 11$ cm pair (upper panel) and $\lambda 6$ cm/ $\lambda 21$ cm pair (lower panel) are shown. The discarded pixels are marked in the small box.

part, especially the western edge (S3 in Fig. 1) with spectral index of $\alpha \sim -0.35$. Slightly flatter spectra were also reported by Leahy & Roger (1998) and Uyaniker et al. (2004) for these regions. The spectral index distribution in general shows a gradual steepening from the south towards the CL 4 region. The maximum spectral difference reaches about $\delta\alpha \sim 0.3$ and is related to a decrease of Cygnus Loop's diffuse radio emission (Fig. 1). It is therefore not clear to what extent the increasing influence of Galactic steep spectrum emission in this region is responsible for the gradual spectral steepening or if it is intrinsic to the Cygnus Loop. This spectral steepening behavior towards the central region with weak diffuse emission is similar seen in the spectral index maps of Uyaniker et al. (2004).

In the shell of the Cygnus Loop shock acceleration might produce high energy electrons and hence strong emission in the presence of a strong magnetic field. The intrinsic spectrum of young electrons at the shock may differ from that in the diffuse emission region in case energetic particles diffuse away and thus steepen the spectrum, as synchrotron aging seems unable to explain a steepening. In regions with weaker magnetic fields the observed emission originates from higher energy electrons. The observed slight flattening in the strongest shell regions is qualitatively understandable. An alternative explanation based on Galactic magnetic field compression was discussed in some detail by Leahy & Roger (1998).

It is obvious that a straight spectrum from integrated flux densities does not rule out variations of the spectrum in different regions of a SNR or a possible spectral steepening in

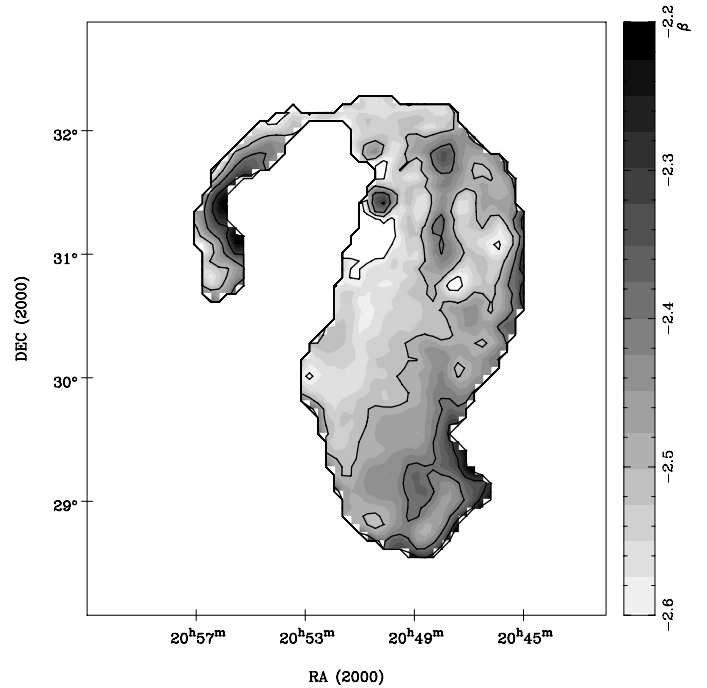


Fig. 7. Spectral index map calculated from $\lambda 6$ cm, $\lambda 11$ cm and $\lambda 21$ cm maps. All the maps are convolved to the angular resolution of $10'$. The gray scale extends from -2.6 (light) to -2.2 (dark) and the overlaid contours start at -2.6 and run in steps of 0.1 .

some areas. To check this possibility, we compare the spectral index maps $\lambda 6$ cm/ $\lambda 11$ cm and $\lambda 6$ cm/ $\lambda 21$ cm. In case the $\lambda 6$ cm/ $\lambda 11$ cm spectral index is smaller than that of $\lambda 6$ cm/ $\lambda 21$ cm a spectral steepening towards higher frequencies is indicated. Otherwise, there is a spectral flattening. We found from the two spectral index maps that in the southern region the spectral indices agree within $\delta\alpha = 0.03$. In the northern part encompassing the central filament, the spectral index of the $\lambda 6$ cm/ $\lambda 11$ cm pair is smaller by $\delta\alpha = 0.1$ than the $\lambda 6$ cm/ $\lambda 21$ cm pair. In the NGC 6992/5 region the spectral index of the $\lambda 6$ cm/ $\lambda 11$ cm pair is smaller at the edge of the rim and larger near the centre. For the rest of the Cygnus Loop the spectral index of the $\lambda 6$ cm/ $\lambda 11$ cm pair is slightly larger, but never exceeding $\delta\alpha = 0.1$. These small spectral differences for different regions suggest that there is no significant spectral steepening or flattening in the frequency range from 1400 MHz to 4800 MHz, even for small regions.

We note that a more detailed TT-plot analysis of the Cygnus Loop for a number of subfields was made by Green (1990), Leahy & Roger (1998) and Uyaniker et al. (2004), where the results from all studies were compared. Large local spectral curvature as reported by Leahy & Roger (1998) was not confirmed by Uyaniker et al. (2004) with high quality data in the frequency range from 408 MHz to 2675 MHz, and also not by us for frequencies up to 4800 MHz.

3.4. Polarization analysis

The polarization intensity maps at $\lambda 11$ cm and $\lambda 6$ cm are very similar in morphology (Figs. 1 and 3). The main polarization

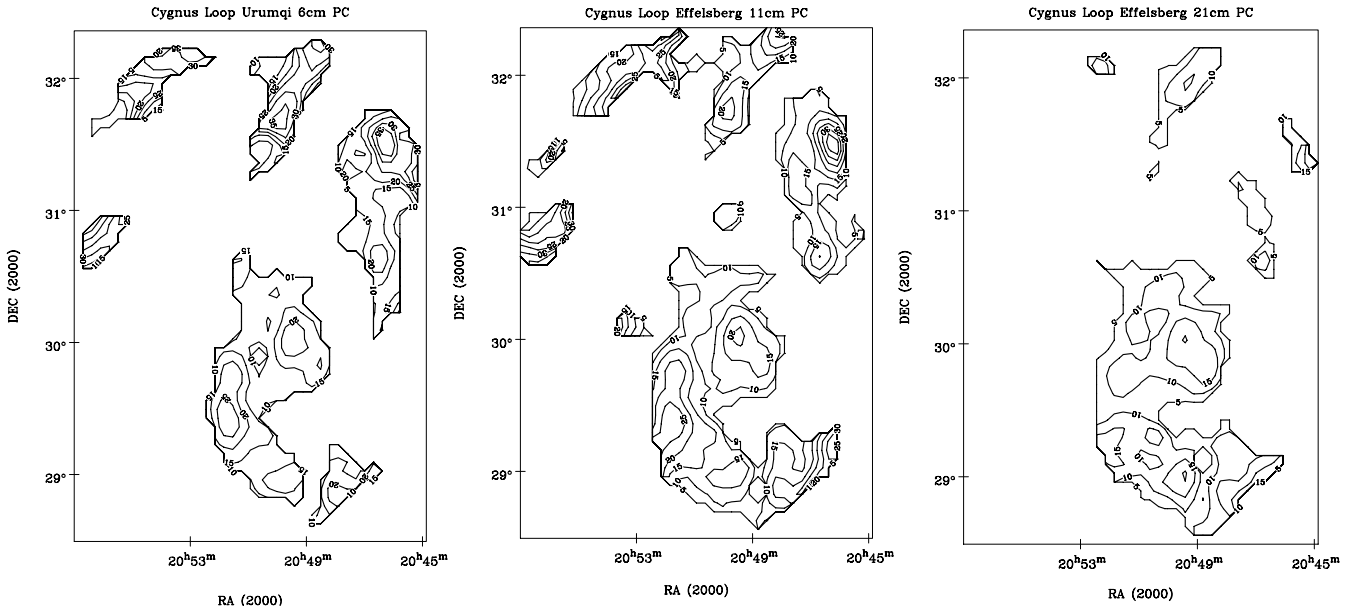


Fig. 8. Polarization percentage at $\lambda 6$ cm, $\lambda 11$ cm, and $\lambda 21$ cm are shown as contours in left, middle and right panels. All the contours start at a level of 5% and run in 5% steps.

features and their nomenclature are displayed in Fig. 1. The polarization percentage (PC) maps derived for these three frequencies are shown in Fig. 8. For total (polarized) intensities below $5 \times (8 \times)$ rms-noise at $\lambda 21$ cm, $5 \times (10 \times)$ rms-noise at $\lambda 11$ cm and $5 \times (20 \times)$ rms-noise at $\lambda 6$ cm no PC is shown.

At $\lambda 6$ cm the central filament C in the northern shell shows strong polarization with polarization percentages up to 35% in the northern shell. The NGC 6992/5 region (NE1 & NE2 in Fig. 1) and the NGC 6960 region (W in Fig. 1) also show a fair amount of polarization up to about 30%. The southern region consists of three patches (Fig. 1: S1, S2 and S3) and all exhibit considerable polarization at a level of about 20%. At $\lambda 11$ cm the percentage polarization is significantly lower in the north than in the south (Uyaniker et al. 2002).

A check on the effect of beam depolarization was made by comparing the Effelsberg $\lambda 21$ cm map with the higher resolution DRAO $\lambda 21$ cm map by Leahy et al. (1997). The DRAO map shows similar very weak polarization in the northern half of the Cygnus Loop, which indicates the presence of strong internal depolarization on scales smaller than resolved by the $1'$ beam of their observations.

3.5. Rotation measure analysis

The polarization maps of the Cygnus Loop maps at three frequencies in principle allow to find out unambiguous rotation measures (RM s). Basically, we linearly fit the polarization angles at three frequencies versus the square of the wavelength for each pixel from all maps. To gain a high signal to noise ratio all pixels with a polarized intensity below $5 \times$ the rms-noise were not included in the fit.

The average RM in the southern region is -21 rad m^{-2} , consistent with earlier results by Uyaniker et al. (2002), Leahy et al. (1997) and Kundu & Becker (1972). The rms-scatter (σ_{RM}) is 7 rad m^{-2} . Such an RM -value at 4.8 GHz results

in a rotation of the polarization angle by roughly 4° with a rms-scatter of about 1.5° . Therefore the $\lambda 6$ cm polarization map quite closely displays the intrinsic magnetic field direction in that region (Fig. 1). The maximum *systematic* uncertainty as inferred by the maximum polarization angle deviations of the calibration sources (1° at $\lambda 11$ cm and at $\lambda 6$ cm), respectively, implies a systematic RM error of up to 4 rad m^{-2} .

The average RM in the central filament C in the northern shell of -28 rad m^{-2} with σ_{RM} of 7 rad m^{-2} is quite similar to that in the southern region.

These RM -values can be attributed to the foreground interstellar medium along the line of sight in the Galaxy: we assume an electron density $n_e \sim 0.02 \text{ cm}^{-3}$, a magnetic field strength along the line-of-sight $B_{\parallel} \sim 3 \mu\text{G}$ as typical values for the local interstellar medium and a distance D of 540 pc. The rotation measure RM calculates: $RM = 0.81 n_e B_{\parallel} D$, which yields an RM of -26 rad m^{-2} , where the negative sign is taken from the general direction of the large scale magnetic field (Han 2004). We note that the Cygnus Loop distance of 540 pc was actually derived from the proper motion of the optical filament in the NGC 6992/5 region (Blair et al. 2005). We use this distance for all components of the Cygnus Loop.

Except for filament C, the RM s in the northern part cannot be derived unambiguously, since at $\lambda 21$ cm the emission is nearly entirely depolarized. For the NGC 6992/5 (NE1/NE2) and NGC 6960 (W) regions polarization angles at $\lambda 11$ cm and at $\lambda 6$ cm are available. The RM ambiguity is $\pm n \times 362 \text{ rad m}^{-2}$. This in principle allows a large number of possible RM s, although values of n larger than 1 seem rather unlikely in view of the physical size of the objects of a few parsec.

We show the minimum absolute RM s ($n = 0$) in Fig. 9. The average minimum RM is about -73 rad m^{-2} for NGC 6992/5 and about -71 rad m^{-2} for NGC 6960. The rms-scatter σ_{RM} is about 31 rad m^{-2} for both regions, much larger than in the southern part. This indicates enhanced fluctuations of the

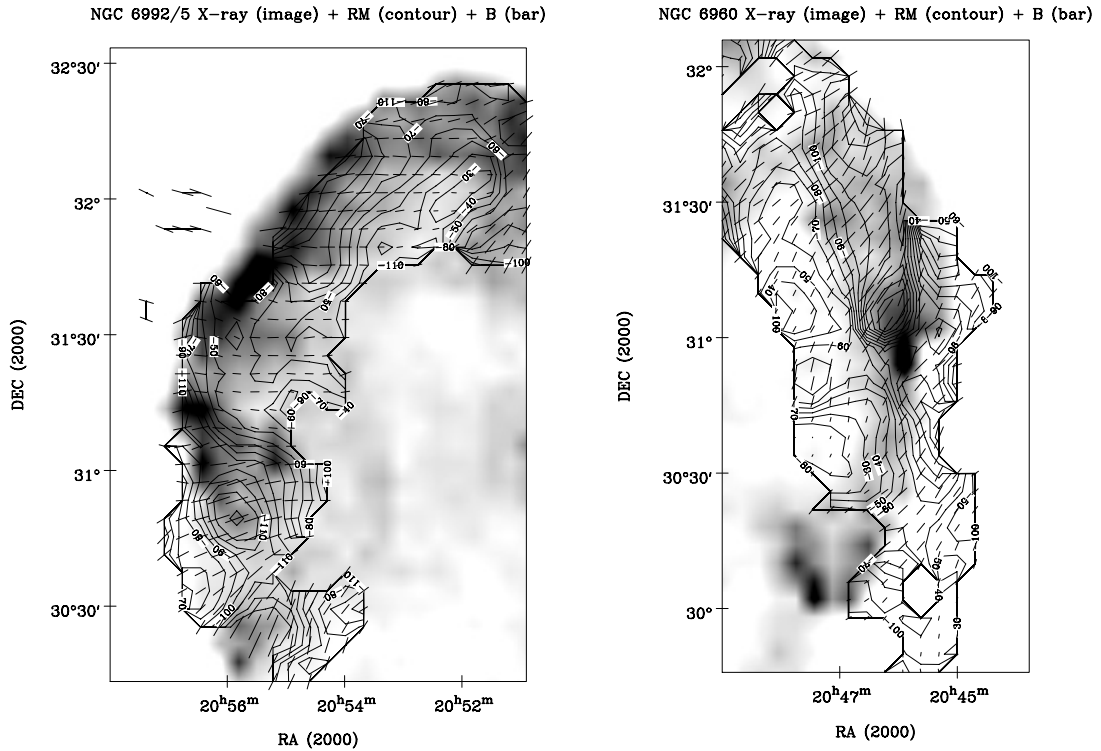


Fig. 9. *RM* maps calculated from the $\lambda 6$ cm and 11 cm maps for the NE1/NE2 and the W region are shown in the left and right panels, respectively. The overlaid grayscale image encodes the 0.25 keV X-ray emission from ROSAT observations (Levenson et al. 1997). The superimposed bars show the intrinsic orientation of the magnetic field.

magnetized interstellar medium in the shells. The large *RM* variation in these regions originates interior to the shell, which is probably caused by the interaction of the blast wave with the cavity wall consisting of a high density cloud (Levenson et al. 1997). Note that the beam of $10'$ corresponds to 1.6 pc at distance of 540 pc, indicating the presence of turbulence in the shock fronts on smaller scales.

Figure 9 shows an intrinsic orientation of the magnetic field in the shell in a more or less radial direction. This is quite unusual for an evolved SNR, where a tangential magnetic field is expected. We therefore analyse also the case of larger *RM* values ($n = \pm 1$). Since the *RM* properties appear similar for NGC 6992/5 and NGC 6960, we will focus on the discussion of NGC 6992/5 for the case of large *RM* values. The mean *RM* ($n = \pm 1$) is about 290 rad m^{-2} (or -430 rad m^{-2}). Such high values of *RM* seem in fact possible when we consider the physical conditions in the shell. The magnetic field can be estimated by assuming energy equipartition between the magnetic field and electrons and protons (Pacholczyk 1970):

$$B_{\min} = C \cdot V^{-2/7} \cdot L^{2/7}. \quad (1)$$

We derive a $\lambda 6$ cm flux density of 11 Jy by integrating the NE1 and NE2 region and calculate the luminosity L for a spectral index of $\alpha = -0.40$. For the radiating volume V we estimate about 400 pc^3 . C is a constant (Pacholczyk 1970).

We obtain an estimate of the magnetic field of $47 \mu\text{G}$ and the line-of-sight component of about $33 \mu\text{G}$ by multiplying the factor of $1/\sqrt{2}$. The typical electron density derived from X-ray observations is a few cm^{-3} with a temperature of about 0.2 keV

from ASCA observations (Miyata et al. 1994). A density of about 1 cm^{-3} in the shell with a similar temperature was derived from ROSAT observations (Lu & Aschenbach 2005). The postshock electron density derived from the optical filament observation is $10\text{--}100 \text{ cm}^{-3}$ (OVI doublet (Long et al. 1992) or SiII (Patnaude et al. 2002)), much larger than that from the X-ray data, although the X-ray emission originates from diffuse gas. With a temperature of 0.1 keV and an electron density of 1 cm^{-3} the pressure is $1 \times 10^{-10} \text{ erg cm}^{-3}$. For a magnetic field of $47 \mu\text{G}$ the pressure is $0.87 \times 10^{-10} \text{ erg cm}^{-3}$, which means a balance between the gas and the magnetic pressure.

Taking the values of the electron density and the magnetic field estimated above and the size of the rim as about 4.8 pc, we calculate an absolute *RM* of 128 rad m^{-2} . This *RM* value shall be taken as a strict lower limit, because the magnetic field can be underestimated by a factor of several due to the unclear filling factor and the electron density is locally definitely much higher than 1 cm^{-3} .

The large *RM*s rotate the $\lambda 6$ cm polarization angles by about 60° and the intrinsic magnetic field direction is in this case along the shell especially for the NE1 knots and for NGC 6960 (Fig. 10), but not for NE2. The NE1/NE2 shell is considerably evolved and has already entered the radiative phase (Danforth et al. 2000). At this stage, the frozen-in interstellar magnetic field is compressed in the shell (van der Laan 1962) and is expected to be tangential to the shock front (Fürst & Reich 2004) as observed.

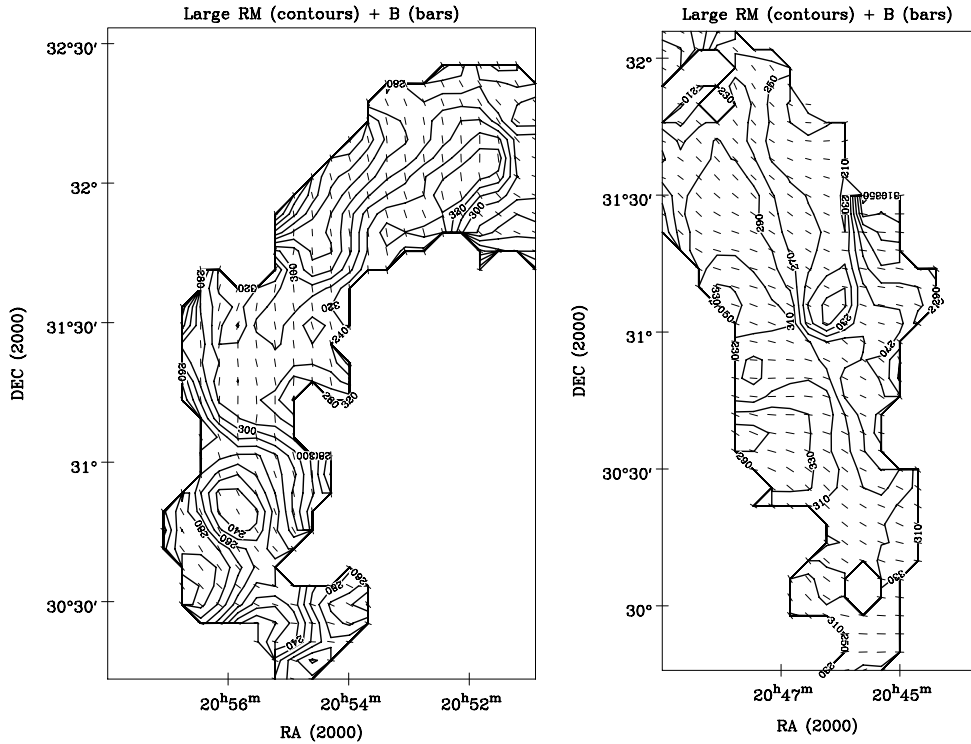


Fig. 10. Rotation Measure in contours and the intrinsic magnetic field in bars for the large RM case is shown.

We conclude that from our estimates large RM values like 290 (-430) rad m^{-2} are quite feasible and in agreement with a basically tangential magnetic field in the shell. The minimum RM value of -73 rad m^{-2} cannot be ruled out, but requires a more radial field configuration, which is typical for rather young SNRs in free expansion. A problem with RM s calculated from two frequencies is that there is no proof of the validity of the λ^2 dependence to extrapolate for intrinsic values. This happens in case the observed polarization at the two frequencies does not originate in the same volume. For a proof, polarization observations higher than 5 GHz are needed.

3.6. Depolarization analysis

The degree of depolarization DP is defined as $DP = PC_o/PC_i$, where PC_o is the observed polarization percentage and PC_i is the intrinsic polarization percentage. For smaller DP the depolarization is more reduced. The caveat here is that DP is wavelength-dependent and PC_i is assumed to be constant for different wavelengths.

There are several mechanisms which could cause depolarization (Burn 1966; Tribble 1991; Sokoloff et al. 1998). One of these mechanisms is *bandwidth depolarization*, which occurs when the polarization angles are rotated by a different amount across the band and hence the observed polarization is reduced. *Bandwidth depolarization* can be written as $DP = \text{sinc}(2RM\lambda^2 \frac{\Delta\nu}{\nu})$, where $\Delta\nu$ is the bandwidth. Another mechanism is *external depolarization*. This is severe in the case of large RM fluctuations (σ_{RM}) in the foreground medium. Different regions of background polarization are rotated to a different extent and reduce the summed polarization signal. The degree of depolarization is directly related to σ_{RM}

as $DP = \exp(-2\sigma_{RM}^2 \lambda^4)$. Finally there is *internal depolarization* which occurs in the emission region. The average of the polarization from different depth and hence with different orientations within the source results in depolarization. In this mechanism DP is given by $DP = |\frac{1 - \exp(-S)}{S}|$, where $S = 2\sigma_{RM}^2 \lambda^4 - 2i\lambda^2 \mathcal{R}$. Here \mathcal{R} is the RM through the entire source, $\mathcal{R} = 2RM$ (Sokoloff et al. 1998). When the variation of RM is very small, the degree of depolarization reduces to $DP = \text{sinc}\mathcal{R}\lambda^2$.

For the southern region the effect of the *bandwidth depolarization* is negligible. With a bandwidth of 20 MHz at $\lambda 21$ cm, 40 MHz at $\lambda 11$ cm, 600 MHz at $\lambda 6$ cm and an RM of -21 rad m^{-2} , a DP of ~ 1 is obtained for all the cases. Internal depolarization seems very small since the RM is mainly of external origin. *External depolarization* does not cause large depolarization due to the small variation of RM . Therefore $PC_{6\text{ cm}} \approx PC_{11\text{ cm}} \approx PC_{21\text{ cm}} \approx PC_i$ is predicted. In fact, we measure similar PCs (Fig. 8) at $\lambda 6$ cm and $\lambda 11$ cm, and a slightly smaller PC at $\lambda 21$ cm map. All measurements are consistent with the expectations.

For the northern part the situation is more complex. Polarized intensities were not detected for NE1 and NE2 and marginally detected for W at $\lambda 21$ cm, which means that $DP_{21\text{ cm}}$ is nearly zero at these regions. The average PC is measured to be about 27%, 28% and 20% for NE1, NE2 and W regions at $\lambda 6$ cm and 23%, 23% and 15% at $\lambda 11$ cm. Here, we investigate the two possibilities for the RM , the small RM case (-70 rad m^{-2}) and the large RM case (290 (-430) rad m^{-2}) to see which can account for the observed depolarization. For both cases the *bandwidth depolarization* is very small. Internal depolarization, therefore, plays an important role since the large RM and RM variation are

caused by a medium interior to the SNR. Leahy et al. (1997) found a correlation between X-ray emission and depolarization, which also indicates the presence of *internal depolarization*. According to that both the large RM case and the small RM case can result in the nearly entire depolarization at $\lambda 21$ cm. An RM of -430 rad m^{-2} , however, can be excluded because this high value of RM makes the polarization even at $\lambda 6$ cm virtually vanish. The small RM can produce DP of $\sim 94\%$, which indicates that the polarization at $\lambda 6$ cm is nearly intrinsic. But a DP of $\sim 50\%$ is then predicted for $\lambda 11$ cm. This means the observed PC at $\lambda 11$ cm is larger than expected. It could well be that the observed polarization originates from different regions along the line of sight at $\lambda 11$ cm and $\lambda 6$ cm, where it might partly come from larger distances than at $\lambda 11$ cm. A large RM of 290 rad m^{-2} , however, causes about 33% of DP at $\lambda 6$ cm, implying an intrinsic polarization of 80% for the NE1 and NE2 regions and 60% for the W region, which is critical although still feasible. The expected PC is also smaller than the observed PC at $\lambda 11$ cm as for the small RM case. We conclude that we cannot infer from the depolarization analysis between the case of large RM or small RM . A definite answer will be given by another high frequency observation or multi-channel narrow band polarimetry.

The central filament shows little depolarization and is salient at all the three wavelengths. This filament is totally different from the other parts in the north in polarization property, which results from its location likely on the surface of the expanding shells.

4. Remarks on the two SNR scenario

Uyaniker et al. (2002) proposed that the Cygnus Loop consists of two SNRs: G74.3–8.4 and G72.9–9.0, where in the centre of G72.9–9.0 the anomalous X-ray source AX J2049.6+2939 is located. It is most likely a neutron star (Miyata et al. 2001) left from the supernova explosion of a $11\text{--}20 M_{\odot}$ progenitor star (Leahy 2004). From the two polarization maps at $\lambda 6$ cm (Fig. 1) and $\lambda 11$ cm (Fig. 3), we can clearly identify two polarized shells corresponding to G74.3–8.4 and G72.9–9.0 with a partial overlap. The polarization properties of these two shells are different. In the southern shell the magnetic field follows the shell conforming to the standard picture of a middle-aged SNR in the adiabatic phase. In the northern part the magnetic field orientation seems to be tangential as well, but the shell structure is more irregularly shaped by the blast wave-cloud interaction. The northern shell is totally depolarized at $\lambda 21$ cm in contrast to the southern shell. Differences between the northern and southern shell are also evident in their X-ray and optical appearance. All the facts above strongly support the two-SNR scenario proposed by Uyaniker et al. (2002).

The relation between these two SNRs is not quite clear as already mentioned by Uyaniker et al. (2002). From our RM analysis the two SNRs are at about the same distance. In the region of overlap there are two regions with enhanced X-ray emission at the western and eastern side (Aschenbach & Leahy 1999; Uyaniker et al. 2002) indicating some interaction between the two SNRs. The spectral index distribution (Fig. 7) shows a weak gradient, but no distinct change. Surprisingly

the X-ray emission does not show any enhancement in the region of overlap (Levenson et al. 1997) as one might expect from the interaction of two shock waves. As already noted by Uyaniker et al. (2002) this is not unique as such an enhancement is also not observed from the interacting SNRs DEM L316 in the LMC (Williams et al. 1997). A more advanced model and further observations of the Cygnus Loop are needed for clarification.

5. Conclusion

We present a new sensitive total intensity and polarization map of the Cygnus Loop at $\lambda 6$ cm, which is the shortest wavelength where a complete map including polarization has been obtained so far. Our highly stable receiver enables us to accurately measure the faint extended emission of the source, which leads to a flux density increase by 20% compared to older data. Our spectral index of $\alpha = -0.40$ for the wavelength range $\lambda 21$ cm to $\lambda 6$ cm is consistent with that found by Uyaniker et al. (2004) for longer wavelengths. This rules out a spectral break in the frequency range between 1.4 GHz to 4.8 GHz. The spectral index maps between different wavelength pairs do not show any spectrum curvature. Some small spatial variations of the spectral index is visible on the combined spectral index map (Fig. 7). The polarization maps support the idea that the Cygnus Loop consists of two SNRs. We derived an RM of -21 rad m^{-2} towards the southern SNR and an RM of -28 rad m^{-2} for filament C. These RM -values are explained by the Galactic foreground emission. The turbulent magnetized medium interior to the northern shell caused by the interaction of a blast wave with a cloud causes total depolarization at $\lambda 21$ cm. The RM of the northern part is based on $\lambda 11$ cm and $\lambda 6$ cm observations. Both a large mean RM of about 290 rad m^{-1} or a small mean RM of about -70 rad m^{-2} seem possible. The larger RM implies a tangential magnetic field for most sections of the shell as expected for an evolved SNR.

Acknowledgements. The $\lambda 6$ cm data were obtained with the receiver system from MPIfR mounted at the Nanshan 25-m telescope at the Urumqi Observatory of NAOC. We thank the staff of the Urumqi Observatory of NAOC for the great assistance during the installation of the receiver and the observations. In particular we like to thank Otmar Lochner for the construction of the $\lambda 6$ cm system and its installation and M. Z. Chen and J. Ma for their help during the installation of the receiver and its maintenance. We are very grateful to Peter Müller for software for mapping observations and data reduction. The MPG and the NAOC supported the construction of the Urumqi $\lambda 6$ cm receiving system by special funds. The research work of XHS and JLH was supported by the National Natural Science foundation of China (10473015) and by the Partner group of MPIfR at NAOC. The support for many bilateral visits by the exchange program between MPG and CAS is appreciated. We thank Nancy Levenson for providing the ROSAT soft X-ray image and Ernst Fürst for critical reading of the manuscript.

References

- Aschenbach, B., & Leahy, D. A. 1999, A&A, 341, 602
- Blair, W. P., Sankrit, R., & Raymond, J. C. 2005, AJ, 129, 2268
- Burn, B. J. 1966, MNRAS, 133, 67

- Condon, J. J., Cotton, W. D., Greisen, E. W., et al. 1998, *AJ*, 115, 1693
- Danforth, C. W., Cornett, R. H., Levenson, N. A., Blair, W. P., & Stecher, T. P. 2000, *AJ*, 119, 2319
- DeNoyer, L. K. 1974, *AJ*, 79, 1253
- Desai, K. M., & Fey, A. L. 2001, *ApJS*, 133, 395
- Emerson, D. T., & Gräve, R. 1988, *A&A*, 190, 353
- Fürst, E., & Reich, W. 1986, *A&A*, 163, 185
- Fürst, E., & Reich, W. 2004, in *The Magnetized Interstellar Medium*, ed. B. Uyaniker, W. Reich, & R. Wielebinski, Copernicus GmbH, 141
- Goss, W. M., van Gorkom, J., & Shaffer, D. B. 1979, *A&A*, 73, L17
- Green, D. A. 1990, *AJ*, 100, 1927
- Han, J. L. 2004, in *The Magnetized Interstellar Medium*, ed. B. Uyaniker, W. Reich, & R. Wielebinski, Copernicus GmbH, 3
- Haslam, C. G. T. 1974, *A&AS*, 15, 333
- Hatchell, J. 2003, APEX-IFD-MPI-0002
- Keen, N. J., Wilson, W. E., Haslam, C. G. T., Graham, D. A., & Thomasson, P. 1973, *A&A*, 28, 197
- Kundu, M. R., & Becker, R. H. 1972, *AJ*, 77, 459
- Leahy, D. A. 2002, *AJ*, 123, 2689
- Leahy, D. A. 2004, *MNRAS*, 351, 385
- Leahy, D. A., Roger, R. S., & Ballantyne, D. 1997, *AJ*, 114, 2081
- Leahy, D. A., & Roger, R. S. 1998, *ApJ*, 505, 784
- Levenson, N. A., Graham, J. R., Aschenbach, B., et al. 1997, *ApJ*, 484, 304
- Long, K. S., Blair, W. P., Vancura, O., et al. 1992, *ApJ*, 400, 214
- Lu, F. J., & Aschenbach, B. 2005, *A&A*, submitted
- Miyata, E., Tsunemi, H., Pisarski, R., & Kissel, S. 1994, *PASJ*, 46, L101
- Miyata, E., Ohta, K., Torii, K., et al. 2001, *ApJ*, 550, 1023
- Pacholczyck, A. G. 1970, *Radio Astrophysics* (San Francisco: W.H. Freeman and Company), 171
- Patnaude, D. J., Fesen, R. A., Raymond, J. C., et al. 2002, *AJ*, 124, 2118
- Sofue, Y., & Reich, W. 1979, *A&AS*, 38, 251
- Sokoloff, D. D., Bykov, A. A., Shukurov, A., et al. 1998, *MNRAS*, 299, 189
- Tenorio-Tagle, G., Różyczka, M., & Yorke, H. W. 1985, *A&A*, 148, 52
- Tribble, P. C. 1991, *MNRAS*, 250, 726
- Uyaniker, B., Fürst, E., Reich, W., Reich, P., & Wielebinski, R. 1999, *A&AS*, 138, 31
- Uyaniker, B., Reich, W., Yar, A., Kothes, R., & Fürst, E. 2002, *A&A*, 389, L61
- Uyaniker, B., Reich, W., Yar, A., & Fürst, E. 2004, *A&A*, 426, 909
- van der Laan, H. 1962, *MNRAS*, 124, 179
- Wang, N., Manchester, R. N., Zhang, J., et al. 2001, *MNRAS*, 328, 855
- Wang, N., Manchester, R. N., Zhang, J., Wu, X., & Esamudin, A. 2003, *Acta Astronomica Sinica*, 44, 207
- Wielebinski, R., Lochner, O., Reich, W., & Mattes, H. 2002, in *Astrophysical Polarized Backgrounds*, ed. S. Cecchini et al., *AIP Conf. Proc.*, 609, 291
- Williams, R. M., Chu, Y.-H., Dickel, J. R., et al. 1997, *ApJ*, 480, 618